

# An introduction to the near real-time QuikSCAT data<sup>\*</sup>

Ross N. Hoffman<sup>†</sup> and S. Mark Leidner<sup>†</sup>

September 24, 2004<sup>‡</sup>

<sup>\*</sup> *Corresponding author address:* Dr. Ross N. Hoffman, Atmospheric and Environmental Research, Inc., 131 Hartwell Avenue Lexington, MA 02421-3126 Email: rhoffman@aer.com.

<sup>†</sup> Atmospheric and Environmental Research Inc., Lexington, MA 02421

<sup>‡</sup> Revised for *Weather and Forecasting*.

## **Abstract**

The QuikSCAT satellite carries the SeaWinds instrument, the first satellite borne scanning radar scatterometer. QuikSCAT which was launched on June 19, 1999, is designed to provide accurate ocean surface winds in all conditions except for moderate to heavy rain (i.e., except for vertically integrated rain rate  $> 2.0 \text{ km mm h}^{-1}$ , the value used to tune the SeaWinds rain flag). QuikSCAT data are invaluable in providing high quality, high resolution winds to detect and locate precisely significant meteorological features and to produce accurate ocean surface wind analyses. QuikSCAT has an 1800 km wide swath. A representative swath of data in the North Atlantic at 2200 UTC 28 September 2000, which contains several interesting features reveals some of the capabilities of QuikSCAT. Careful quality control is vital to flag data that are affected by rain and to flag errors of ambiguity removal. In addition, an understanding of the instrument and algorithm characteristics provides insights into the factors controlling data quality for QuikSCAT. For example data quality is reduced for low wind speeds, and for locations either close to nadir or to the swath edges. The special data characteristics of the QuikSCAT scatterometer are revealed by examining the likelihood or objective function. The objective function is equal to the sum of squared scaled differences between observed and simulated normalized reflected radar power. We present typical examples and discuss the associated data quality concerns for different parts of the swath, for different wind speeds, and for rain versus no rain.

# 1. Introduction

The primary mission of the SeaWinds instrument on the QuikSCAT satellite is to retrieve the surface vector wind over the global ocean (Lungu 2001). QuikSCAT wind vectors are generally of high quality, but error characteristics are complex. The two goals of this paper are to show how well the high quality, high resolution QuikSCAT data depict the ocean surface wind field, and to provide some insight into the data errors. We will illustrate the types of errors that occur due to rain contamination and ambiguity removal. We will also give examples of how the quality of the retrieved winds varies across the satellite track, and how it varies with wind speed.

SeaWinds is an active, Ku-band microwave radar operating at 13.4 GHz. Centimeter-scale gravity or capillary waves on the ocean surface reflect (i.e., backscatter) the radar power primarily by means of the Bragg resonance process. These waves are usually in equilibrium with the wind. The crests and troughs of the small scale waves tend to be aligned perpendicularly to the wind direction. This results in a modulation of the observed backscatter with the wind direction. Thus backscatter measured by scatterometers contains information about the vector wind. The vector wind is determined by combining several backscatter observations made from multiple viewing geometries as the scatterometer passes overhead. At each geographic location or wind vector cell (WVC), usually two, three, or four wind solutions are found to be consistent with the observed backscatter. The WVC resolution is 25 km. Each radar backscatter observation samples a patch of ocean about  $25 \times 37$  km. (See Section 2 for a description of the SeaWinds instrument and wind retrieval.)

In addition to wind speed and direction, other factors can influence backscatter observations and thereby affect the retrieved winds. The most important of these is rain. Rain changes the ocean surface roughness, and attenuates and scatters the radar energy. QuikSCAT is designed to provide accurate ocean surface winds in all conditions except for moderate to heavy rain defined as vertically integrated rain rate  $> 2.0 \text{ km mm h}^{-1}$ . This value of rain rate and estimates from collocated SSM/I observations were used to tune the SeaWinds rain flag. Even with rain free backscatter observations, the quality of retrieved winds varies with several factors. Light winds are troublesome, since the ocean surface acts more like a smooth reflector than a scatterer. Direction errors decrease with increasing wind speed. The measurement geometry of SeaWinds results in

error characteristics which vary across the satellite swath. Errors are smallest in an optimum region of the swath, termed the mid-swath or “sweet spot”, away from nadir and the far edges of the swath. Data are processed in segments. Inconsistencies can arise in regions of overlap between segments.

In this paper, we use a single swath of data over the North Atlantic to illustrate the benefits and potential pitfalls of vector winds from QuikSCAT (Section 3, Section 4 and Section 5). The examples presented should improve everyday use of the data, both qualitative and quantitative, through a deepened understanding of the instrument, its principles of operation, and the method of determining vector winds. In this paper, we use only the near real-time (NRT) QuikSCAT data produced by NOAA/NESDIS and distributed to operational users in BUFR format (Thorpe 1995). A different science data product (SDP) is created by JPL and distributed by PO.DAAC in delayed mode in HDF format. Most published work makes use of the SDP. The important differences between the two data sets are listed in Section 2. We conclude with a short review of the current and potential uses of QuikSCAT data (Section 6) and a summary (Section 7).

## **2. The QuikSCAT scatterometer and processing algorithms**

This paper describes the attributes of the NRT QuikSCAT data. These data are produced at NOAA/NESDIS with a 3 hour latency goal. This is a very stringent goal and almost all data are available within 3.5 hours. To meet these requirements the QuikSCAT NRT data processing algorithms combine the finest grained  $\sigma^0$  measurements into fewer composites than the science data algorithms. Otherwise the QuikSCAT NRT processing algorithms are identical to the science data algorithms (Lungu 2001). There are also two differences in how the processing algorithms are implemented. First, data are grouped by segments by the NRT system and by “revs” by the SDP system (Section 2.f). Second NCEP forecasts initialize the ambiguity removal in the NRT system, while the SDP system uses NCEP analyses. The forecasts used are NCEP global operational forecasts from the Global Forecast System (GFS) model and are typically 6–9 hours old. Previous to 6 March 2002 the GFS was run with two data cutoff times resulting in an early aviation (AVN) run and a later medium range forecast (MRF) run. QuikSCAT NRT processing used AVN forecasts before GFS replaced AVN and MRF was terminated. The QuikSCAT NRT system is described by Augenbaum et al. (2004, and references therein).

Collocation studies show that if the ambiguity is properly resolved, scatterometer data are very accurate (Bourassa et al. 1997; Stoffelen 1998; Atlas et al. 1999; Freilich and Dunbar 1999; Wentz and Smith 1999). Collocation studies by Bourassa et al. (2003) for QuikSCAT suggest comparable accuracy to the NASA Scatterometer (NSCAT). Studies cited here are for SDP, but similar results would be expected for the NRT data since the SDP and NRT agree so closely. For example, we found rms differences between SDP and NRT data of only  $0.49 \text{ m s}^{-1}$  for wind speed and  $23^\circ$  for wind direction for the more than 10 million rain free pairs collected from 30 October to 12 November 2001 (Leidner et al. 2001). Data from the far swath were excluded in this collocation, and approximately 4% of all the pairs were eliminated due to rain flags. NRT quality is significantly worse than SDP quality in the far-swath primarily because the NRT wind inversion operates on only two  $\sigma^0$  composites for these WVCs (Scott Dunbar, pers. comm.). With this exception, the NASA/JPL QuikSCAT Project team found generally minor differences when comparing SDP and NRT data, and consequently authorized public release of the NRT data in January 2000.

#### *a. Timeline*

The SeaWinds instrument on QuikSCAT was launched 7:15 p.m. Pacific Daylight Time on 19 June 1999 by a U.S. Air Force Titan II launch vehicle from Vandenberg AFB. SeaWinds was turned on 7 July and QuikSCAT achieved its operational inclined polar orbit, 803 km above the earth on 10 July. Each orbit is  $\approx 100$  minutes long and the spacecraft travels at  $\approx 7 \text{ km/s}$ . There are about 15 orbits per day or about 100 per week, and equatorial crossing points or nodes are separated by 2800 km. Every 57 orbits is a repeat. The orbital plane is perpendicular to the sunlight and local time at the ascending node is within 30 minutes of 0600. The spacecraft is rarely in the earth's shadow. The first scientifically valid QSCAT winds were acquired from rev 430 at 1839 UTC on 19 July 1999. Note that QuikSCAT *orbits* start at the ascending node and QuikSCAT *revs* (short for revolutions) start at the ground track location closest to the South Pole.

Since its launch, the SeaWinds instrument has produced ocean surface wind vectors reliably. The QuikSCAT swaths cover over 90% of the earth's surface in 24 hours. QuikSCAT spatial coverage is similar to other sun synchronous polar orbiting satellite instruments with complete 24 hour coverage except for small polar cap regions and irregularly spaced diamond shaped data gaps

equator-ward of  $45^\circ$  (Fig. 1). Such areal coverage, reliably available since the launch of QuikSCAT, was not at all possible before the advent of space based scatterometers. Data outages have been short or infrequent. Data gaps can be foreseen when the instrument is put in standby mode and the spacecraft is reoriented to minimize its cross-section for Leonids meteor showers. This occurred in 1999, 2000, 2001, and 2002, but not in 2003 when the predicted risk was much smaller. There is a tendency for unplanned data gaps to occur on holidays and weekends. For example there was a gyroscope failure on 1 January 2000. The other notable instrument failure was of a GPS receiver on 11 May 2001. Some anomalies might have been avoided: There are gaps associated with inadequate quality control early in the mission on 20 July 1999, with an attempt to update the star catalog on 20 August 2002, and with a poorly timed downlink during the peak eclipse period on 18 December 2003 when the battery charge was low. Other notable gaps occurred on 20 January 2000 and 4 July 2002 due to system resets, on 18 July 2000, 7 July 2001, and 29 May 2003 due to spacecraft data bus failures, on 19 March 2002 due to an attitude control anomaly, and on 28 August 2000, and 11 September 2003 due to GPS anomalies. Some of these occurrences may be due to cosmic rays over the South Atlantic Anomaly (Heirtzler 2002). In all cases the QuikSCAT team responded rapidly and effectively to restart useful data acquisition. In fact data gaps account for less than 1.2% of the total time between revs 430 when data acquisition began and rev 23970 when we made the calculation.

Marine Prediction Center forecasters had access to preliminary QuikSCAT data as early as August 1999 (Atlas et al. 2001). This group, now called the Ocean Prediction Center, has used QuikSCAT data extensively since July 2001 (<http://www.opc.ncep.noaa.gov/quikscat/>). A NOAA/NESDIS web site (<http://manati.wwb.noaa.gov/quikscat/>) has displayed the QuikSCAT NRT winds since the general release of QuikSCAT data on 31 January 2000 by JPL. The NRT QuikSCAT BUFR data (Leidner et al. 2000) were first distributed to the operational community 23 February 2000. Rainflags were added to the BUFR data in mid June 2000. Hurricane forecasters began using QuikSCAT data for the 2000-2001 hurricane season to aid detection of new tropical cyclones (Sharp et al. 2002). NRT QuikSCAT data have been assimilated by the global analyses at NCEP since 1200 UTC 15 January 2002, and at ECMWF since 1800 UTC 21 January 2002. At the NASA Data Assimilation Office QuikSCAT data were first assimilated in June 1999, and operationally in

real time in August 2001. Beginning in March 2004, QuikSCAT data become available at U.S. NWS forecast offices with the installation of a recent build of the Advanced Weather Interactive Processing System (AWIPS). (The AWIPS home page is [http://199.26.34.19/AWIPS\\_home.html](http://199.26.34.19/AWIPS_home.html).)

Another SeaWinds instrument was launched on the ADEOS-2 (later renamed Midori-2) spacecraft in December 2002. Unfortunately contact with the spacecraft was lost in October 2003 before the NRT data became available operationally.

*b. Principles of operation*

SeaWinds on QuikSCAT is the first scatterometer using a rotating antenna to be flown in space (see Fig. 2). Microwaves are transmitted to the surface in two pencil beams (see Fig. 3). Then, SeaWinds measures the reflected power from the earth's surface at the satellite (Spencer et al. 2000). The ratio of the transmitted power to the received power, called the normalized radar cross section or NRCS or backscatter, and denoted  $\sigma^0$ , is the fundamental measured quantity. As the instrument's 1-meter dish rotates at 18 rpm, the two pencil beams oversample an 1800 km wide swath on the earth's surface with both forward- and aft-looking measurements. Foreward and aft refer to beam footprints foreward and aft of the spacecraft. Thus the backscatter values at a single location are observed within a time span of up to 290 seconds, increasing as the location approaches nadir. There are four types of measurements or "flavors"—inner-foreward, outer-foreward, inner-aft, and outer-aft. The QuikSCAT NRT data contain one composite value for each flavor for each WVC. Here inner and outer refer to the inner and outer scan beams with look angles of  $39.876^\circ$  and  $45.890^\circ$  resulting in approximately constant incidence angles at the earth's surface of  $45^\circ$  and  $53.6^\circ$ , respectively. Inner and outer beams are horizontally and vertically polarized, respectively. This diversity of measurements improves the ability of SeaWinds to determine wind direction. Note that in the far-swath there are only outer beam footprints, and thus only two flavors of  $\sigma^0$ . QuikSCAT NRT wind inversion requires at least one foreward beam measurement and at least one aft beam measurement.

Since there are nominally four flavors of  $\sigma^0$  values in the center of the swath, but only two in the far-swath, wind retrievals in the far-swath are expected to be of lower quality. Further, we may identify two zones within the inner-swath, which we call the mid-swath and nadir-swath,

of greater and lesser quality, respectively. The mid-swath ( $\approx 200 - 700$  km on either side of the satellite track) has the greatest diversity of azimuth and incidence angles, and hence the best quality data. The mid-swath is also known as the “sweet spot”.

*c. The wind vector cell (WVC) grid*

The QuikSCAT data are organized in a swath-based format. Each WVC in the entire QuikSCAT mission may be uniquely identified by three numbers, the along track position or row number, the across track position or cell number, and the rev number. There are 76 cross track cells. For each cell, there are 1624 rows of WVCs, from the beginning to the end of each rev. Unlike NSCAT, there is no “nadir” gap for QuikSCAT. The nominal instrument measurement swath extends 900 km to either side of the nadir track. Thus, 36 cells on either side of nadir, should accommodate nearly every  $\sigma^0$  measurement. Variations in spacecraft attitude and the local curvature of the earth will cause very few  $\sigma^0$  measurements to fall outside of the nominal measurement swath. To accommodate these measurements, the QuikSCAT data products include two additional “guard” cells on either side of the measurement swath, for a total of 76 cross-track cells. The boundary between mid-swath and far swath is 700 km at the nominal limit of the coverage of the inner antenna. The boundary between nadir swath and mid-swath is somewhat arbitrarily defined at 200 km from nadir. Thus cells 31–46 are in the nadir swath, cells 11–30 and 47–66 are in the mid-swath, and cells 3–10 and 67–74 are in the far swath. Cells 1–2 and 75–76 are the aforementioned “guard” cells that should never contain enough  $\sigma^0$  measurements to determine wind vectors.

*d. Wind inversion*

Wind inversion is the first step of the wind retrieval process. This first step inverts the geophysical model function (e.g., Freilich and Dunbar 1993; Wentz and Smith 1999) for a given set of  $\sigma^0$  values to obtain multiple maximum likelihood estimates of the wind speed and direction. To complete the wind retrieval process an ambiguity removal algorithm selects one of these estimates (or ambiguities) at each WVC (Section 2.e). While the first order response of backscatter is a power law in wind speed, it is the modulation of this response by wind direction that creates ambiguity in the wind inversion. The wind direction modulation approximately follows the cosine of twice the



relative azimuthal angle between the wind direction and the antenna direction (projected onto the ocean surface). This harmonic response in turn gives rise to the  $180^\circ$  ambiguity in winds consistent with the  $\sigma^0$  measurements in a WVC. It is for this reason that the inversion process, performed in a point-wise fashion (assuming each WVC is independent of its neighbors), yields multiple solutions or ambiguities.

Wind inversion determines the scatterometer wind ambiguities as the multiple minima of an objective function which measures the squared difference between observed and simulated backscatter. The objective function is described in more detail in the Appendix. The rank one ambiguity is the solution associated with the smallest value of this objective function. The rank two ambiguity is the solution associated with the second smallest value of this objective function, and so on. The simulated backscatter or  $\sigma^0$  is determined by a geophysical model function,  $F$ ,

$$\sigma^0 = F(\mathbf{V}; \alpha, \theta, f, p). \quad (1)$$

Here  $\mathbf{V}$  is the wind vector,  $\alpha$  is the azimuth angle and  $\theta$  is the incidence angle of the observation,  $f$  is the frequency (13.4 GHz for QuikSCAT), and  $p$  is the polarization. The geophysical model function developed for NSCAT (Wentz and Smith 1999) has been adjusted for SeaWinds (Lungu 2001). The model function is the most accurate for wind speeds in the range  $5 - 12 \text{ m s}^{-1}$ . Therefore errors are larger at higher and lower wind speeds outside this range.

Equation (1) neglects the effects of other parameters, notably rain. Rain changes the usual ocean surface (Sobieski et al. 1999), and at 13.4 GHz rain attenuates and scatters the radar energy (Draper and Long 2004). Errors may be very large for rain contaminated WVCs. New model functions are being developed and tested that include the effects of rain and allow for the simultaneous inversion for wind vector and rain rate (e.g., Draper and Long 2004).

Other parameters may affect the relationship between wind vector and backscatter, but these probably have a small impact in terms of magnitude or come into play rarely (Brown 1983; Quilfen et al. 2001). For example, temperature and salinity have small effects on viscosity of ocean water and thus on the generation of small scale surface waves by the wind. On the other hand, surface contaminants such as an oil spill may greatly affect the generation of small-scale surface waves, but only rarely. In principle, large swell or rapidly changing winds should also affect the ocean surface and hence  $\sigma^0$ . Note that  $\mathbf{V}$  in (1) is the neutral stability wind at 10 m, and winds determined

using this relationship will differ from the actual winds due to stability effects (Hoffman and Louis 1990). Over the oceans, conditions are often close to neutral stability. In extreme conditions, say in association with strong outflow from a land mass, the difference between the actual wind and the neutral stability wind can be noticeable, especially for unstable conditions and low wind speeds. For example a neutral wind of approximately  $5.4 \text{ m s}^{-1}$  corresponds to an actual wind of  $5.0 \text{ m s}^{-1}$  if the air is colder than the sea by  $2^\circ\text{C}$  for typical conditions, and to an actual wind of  $5.6 \text{ m s}^{-1}$  if the air is warmer than the sea by  $2^\circ\text{C}$  (Mears et al. 2001, Fig. 1). Also  $V$  is relative to any ocean currents (e.g., Cornillon and Park 2001). For example, an  $8 \text{ m s}^{-1}$  wind over a  $1 \text{ m s}^{-1}$  ocean current, both flowing in the same direction, appears to the scatterometer as a  $7 \text{ m s}^{-1}$  wind since it is the wind relative to the surface that generates the small scale waves.

#### *e. Ambiguity removal*

After wind inversion, an ambiguity removal algorithm selects one solution at each WVC by requiring horizontal consistency and/or consistency with *a priori* information. Note that the process of ambiguity removal is performed in a field-wise fashion. The operational algorithm used by QuikSCAT is a vector median filter (Shaffer et al. 1991). The median filter is initialized with the ambiguity closest to a short term (usually 6–9 hours old) numerical weather prediction from the NCEP GFS. In the rare instances when the NRT system cannot locate a current forecast ( $< 12$  hours old) the median filter is initialized with the first ambiguity. Since the first or second ambiguity is correct most of the time, the initialization is restricted to one of these. On each pass of the median filter at each WVC the ambiguity closest to the median of the currently selected wind vectors in a  $7 \times 7$  neighborhood of WVCs is chosen. Here closest is defined in terms of the smallest magnitude of the difference between the two vectors being compared. The median filter will preserve fronts but eliminate individual wind vectors that do not agree with neighbors. (To see how a median filter preserved fronts consider an idealized discontinuity on a grid with all points on the right having a value one and all points on the left having a value zero. A median filter will reproduce such a field exactly since the median value in each  $7 \times 7$  neighborhood will be the value (one or zero) in the majority.) For the QuikSCAT SDP Draper and Long (2002) estimated that ambiguity removal is correct 95% of the time. We expect that the ambiguity removal skill for

the NRT QuikSCAT data is similar since we found such good agreement between the NRT and SDP winds (Leidner et al. 2001). Since the selected winds are horizontally consistent, ambiguity removal errors tend to occur in patches or lines. Incorrect ambiguity removal results in large wind direction errors (often  $\approx 180^\circ$ ), but does not result in larger than normal wind speed errors.

Ambiguity removal skill varies across the swath. Our ability to retrieve the ocean surface wind vector increases with increasing diversity of the viewing geometries of the measurements obtained for a WVC. Measurement diversity is lower at nadir and in the far swath compared to the intervening “sweet spots”. At least two techniques have been proposed to account for the relative lack of directional information in parts of the swath, but have not been implemented for NRT processing. The general idea is to explicitly account for the larger uncertainty in direction near nadir and in the far swath (e.g., Stiles et al. 2002; Portabella and Stoffelen 2004).

*f. Edge effects and overlap*

Ambiguity removal sometimes fails near the edge of a swath. Two factors make the edge a difficult region. First, the median filter has fewer neighboring points to use, and those that are available are primarily on one side of the point being filtered. Second, the far swath has less diversity. It contains only vertically polarized observations and as the swath edge is approached the viewing geometry for fore and aft beams becomes virtually the same.

The NRT data have another edge that is not present in the science data. The science data are processed a rev at a time. As a result the discontinuity between revs falls over Antarctica where there are no ocean winds to retrieve. The NRT data are processed by data segments whenever sufficient data become available. A data segment is composed of all data collected during a time interval prior to downlink. Figure 1 highlights a single data segment. Data segments are made to overlap by buffering the latest data that has already been processed. Nominally this overlap is 15 minutes. An overlap is required because at the ends of the segments some backscatter values will be missing. (For example, the forward beam measurements will be missing at the start of a segment.) Therefore ambiguity removal at the ends of the segments will face the same problems as at the swath edge or near a coastline. Since wind retrieval requires at least one forward and one aft measurement there is a characteristic pattern of WVCs containing retrieved winds at the end of

a segment (Fig. 1). To minimize edge effects the ends of segments should be trimmed at the WVC rows near the midpoint of the temporal overlap. These boundaries are shown for the highlighted segment in Fig. 1. At the beginning of this segment in the South Indian Ocean there is an overlap of 38 minutes, but at the end of the segment in the South Pacific there is only a 10 minute overlap.

In the overlap region between segments there may be inconsistencies between the ambiguities selected independently for each segment. This could result in a discontinuity in wind direction where the two segments meet. Similar discontinuities should be expected when orbits overlap. (The chance for overlapping orbits increases towards the poles and with longer time windows.) In addition to differences in ambiguity selection successive orbits should be expected to exhibit temporal changes.

### **3. A representative swath of QuikSCAT data**

To illustrate features and uses of the data, we chose an interesting swath of data over the North Atlantic. All of our examples are taken from this single swath of data collected from 2200 through 2215 UTC 28 September 2000 during the descending pass of QuikSCAT rev 6659. Figure 4 shows the selected wind vectors (thinned, for clarity, to every fourth WVC along- and across-track) over on a GOES satellite infrared image valid 2215 UTC 28 September 2000. Winds contaminated by rain according to the NRT rain flag are plotted in green. Very low wind speed cases discussed later (in Section 5.c) are highlighted with red. The NCEP GFS mean sea-level pressure analysis valid at 0000 UTC 29 September is also plotted to corroborate features in the satellite data. Synoptic-scale features may be easily observed in QuikSCAT wind fields. The example swath includes Hurricane Isaac near its peak intensity. Easterly winds are evident in the tropics in the scatterometer winds. North of Isaac, scatterometer winds show anticyclonic flow around the two high pressure systems separated by a wind shear front. This front is associated with a trough in the NCEP GFS surface pressure field and a cloudy area in the GOES image. Note that some areas in far swath are not consistent with the rest of the data. For example near 15°N on either side of the swath.

Figure 5 shows hurricane Isaac only and scatterometer winds at full 25 km resolution. At 1800 UTC the best track (<http://www.nhc.noaa.gov/2000isaac.html>) indicates Isaac's position at 26.6°N 54.2°W with an estimated minimum central pressure of 943 hPa, and maximum sustained

winds of  $62 \text{ m s}^{-1}$  (120 kt). Isaac's motion at 1800 UTC was toward  $325^\circ$  true north at  $9 \text{ m s}^{-1}$  (17 kt). Six hours later Isaac was at  $28.0^\circ\text{N } 55.1^\circ\text{W}$ , and had weakened to 948 hPa, with maximum sustained winds of  $59 \text{ m s}^{-1}$  (115 kt). The eye diameter is estimated to be approximately 46 km (25 n mi). The center passed about 815 km (440 n mi) east of Bermuda during 29 September. The distribution of wind speed, but not direction, around Isaac as observed by QuikSCAT in Fig. 5 is in very good agreement with the position in the GOES image. There is even a minimum in scatterometer wind speed in the eye of the hurricane (a  $23 \text{ m s}^{-1}$  (45 kt) wind surrounded by an annulus of winds  $31 \text{ m s}^{-1}$  (60 kt) or greater coincident with the relative minimum in infrared temperature near  $27.5^\circ\text{N } 55^\circ\text{W}$ ). However, the choice of wind direction by ambiguity removal is clearly in error near the center of the storm. Also, the maximum wind speed observed by the scatterometer is  $36.4 \text{ m s}^{-1}$  (71 kt), only 60% of the estimated maximum sustained winds at the time.

Problems with ambiguity removal due to rain contamination and underestimation of very high wind speeds are common in scatterometer data around intense tropical cyclones. Special approaches to these problems have been studied by Jones et al. (1999) and by Yueh et al. (2001). Ambiguity removal problems can be addressed by variational data assimilation schemes (e.g., Hoffman et al. 2003; Leidner et al. 2003, also see Section 4). Current scatterometer model functions have been trained using very few high winds as ground truth. On-going efforts will continue to collect high quality collocation data in hurricane conditions from aircraft using new instruments such as the stepped-frequency microwave radiometer (Uhlhorn and Black 2003). In the future these data will improve scatterometer model functions for high wind conditions. In spite of these shortcomings, the sampling of surface winds by scatterometer has great value in defining the center, asymmetries in the circulation, and the surrounding environment of a tropical cyclone.

Figure 6 shows a large-scale, stationary synoptic front and scatterometer winds at full 25 km resolution. Surface winds are somewhat chaotic in the cloudy frontal region between the two centers of high pressure (to the northwest and southeast). The GOES satellite image shows embedded regions of convection in this area. As seen in the NCEP GFS MSLP analysis, there are two lobes of low pressure within the associated trough. There are rain flags set for a number of wind vectors in this region. We know (Hoffman et al. 2004) that the current QuikSCAT rainflags are overly con-

servative for high winds. For Isaac (Fig. 5) many of the flagged wind vectors are consistent with the presence of a hurricane and are probably good. But the block of vectors in the center of Fig. 5 that have a cross-track orientation is very probably due to rain contamination. In Fig. 6 the rain flags seem generally correct. The winds flagged here have anomalously high speeds, a cross-track orientation, or both; or are immediately adjacent to such winds. More on the effect of rain flags on the the use of the data will be shown in Section 4 and the effect of rain contamination on wind inversion will be presented in Section 5.d.

## 4. An analysis impact example of QuikSCAT data

Here we show an example of the impact of QuikSCAT data on the analysis of ocean surface winds. We use a variational data assimilation method for two-dimensional wind fields, 2d-VAR. As in all variational assimilation schemes, 2d-VAR combines observations and an *a priori* or first guess estimate of the solution. The analysis is found through a minimization procedure that balances the fit to observations with meteorological constraints on the solution. For a full description of the technique and applications of 2d-VAR see Hoffman et al. (2003) and Henderson et al. (2003).

The 2d-VAR analysis region is the area depicted in Fig. 4. The analysis grid is a  $1^\circ \times 1^\circ$  latitude/longitude grid (i.e., no map projection). The 2d-VAR uses all available QuikSCAT data at 25 km resolution within the area of Fig. 4 from rev 6659. A three-hour NCEP GFS forecast provides the background wind field and is valid at 2100 UTC 28 September. We chose a short-term forecast closest in time to the scatterometer observations for the background, since this is the practice at many operational centers. The results of two analyses are presented here: ALLOBS uses all available observations in the region ( $N = 12004$ ), while NORAIN uses only those observations free from rain contamination ( $N = 10754$ ). Both experiments use all winds solutions at each data point, and 2d-VAR chooses one during the analysis. (During the initial phase of the analysis only the most likely ambiguity and the ambiguity most nearly opposite are used. For more information on QC methods for ambiguous scatterometer winds see Hoffman et al. (2003).)

The overall impact of 2d-VAR may be seen by comparing the observations to the background and then to the analysis. Histograms of wind speed differences are shown in Fig. 7 for the NORAIN analysis. In the mean, the scatterometer winds are  $0.4 \text{ m s}^{-1}$  higher than the NCEP back-

ground winds with a standard deviation of the differences of  $1.8 \text{ m s}^{-1}$ . Relative to the analysis, the scatterometer winds are only  $0.2 \text{ m s}^{-1}$  higher with a standard deviation of the differences of  $1.3 \text{ m s}^{-1}$ . Therefore, 2d-VAR has created a surface wind analysis which better fits the scatterometer data. A similar result is found for the ALLOBS analysis, but rain contamination increases both the mean and rms differences for comparisons with both background and analysis (see Table 1).

It should be noted that scatterometer winds are generally higher than winds from global forecast models both in the mean and for extreme cases. This may be due to the difference in scales represented and to the inexact representation of the boundary layer and surface exchanges in global models (Brown 2002). For example Yu and Gerald (2004) report that on average GFS analysis surface winds are  $0.55 \text{ m/s}$  slower than deep water buoys.

Scatterometers have the ability to detect mesoscale features which may not be present in large-scale analyses (Peteherych et al. 1981; Atlas et al. 1999, 2001). Figure 8 depicts just such a case. QuikSCAT detected a small circulation embedded in the southern lobe of low pressure in the synoptic trough. Figure 8 top left panel shows the NCEP background wind field (streamlines and wind barbs) in the vicinity of the trough. The NCEP 3-hr forecast has simple shearing flow along the front. All QuikSCAT ambiguities within the area of the orange dashed box in this panel are shown in the top right panel over the GOES imagery. Here green indicates a rain flagged WVC. Notice the data gap around Bermuda in the SW corner of this panel. Since  $\sigma^0$  measurements close to land are a mixture of land and ocean signals, winds are not calculated within 30 km of land. The panels in the middle row show in a similar format the ALLOBS analysis and the ambiguities closest to this analysis, and the bottom row shows the NORAIN analysis and the ambiguities closest to NORAIN. In the NORAIN analysis, a closed circulation is found along the front, consistent with the ambiguities in the lower right panel of Fig. 8. While only the possibility of this feature is suggested by the NCEP MSLP analysis, the presence of a closed circulation is supported by a time series of succeeding MSLP analyses (not shown). The ALLOBS analysis is very poor since rain-contaminated data indicated by green wind symbols in the figure are used. Within the rain contaminated area there are many examples of WVCs with triplets of wind ambiguities directed east, *north*, and west adjacent to WVCs with wind ambiguities directed east, *south*, and west (e.g., at  $34^\circ\text{N } 63^\circ\text{W}$ ). To fit these data the analysis must be eastward or westward. In addition errors in



wind speed in the areas of heavy rain make them unsuitable for use in data assimilation.

## 5. Factors influencing QuikSCAT data quality

Careful quality control is vital to consistently obtain high quality results. Understanding of the instrument and algorithm characteristics provides insights into the factors controlling data quality for QuikSCAT. In Section 2 we briefly described the viewing geometry, the effect of rain, and the accuracy of QuikSCAT winds. In this section we reprise each of these in more detail with regard to potential effects on data quality. We present typical examples of data and discuss the associated data quality concerns, for different parts of the swath, for different wind speeds, and for rain versus no rain. The objective function for representative WVCs presented here graphically illustrate the workings of the wind inversion algorithm.

### *a. Scatterometer objective functions and wind inversion*

Many of the special data characteristics of a scatterometer are revealed by examining the likelihood function that is maximized during the wind inversion. In QuikSCAT processing, various approximations make the process of maximizing the likelihood equivalent to minimizing an objective function which is equal to the sum of squared scaled differences between observed and simulated backscatter. Each difference is scaled by its expected error. The objective function is precisely defined in the Appendix.

The nature of the ambiguity of scatterometer data is apparent when the objective function is plotted with respect to the values of the  $u$  and  $v$  wind components. Because the objective function has such a large range, we plot only selected contours—1, 2, 3, 5, 7 in blue, 10, 20, 30, 50, 70 in green, and 100, 200, 300, 500 in orange. Values 700 and higher are filled in with red. A typical example taken from QuikSCAT rev 6659 at row 1100 and cell 18 is shown in Fig. 9.a.

In order to make sense of this plot and subsequent ones in the manuscript, consider the progression of the other panels in Fig. 9. First consider Fig. 9.b showing the result of using just one backscatter measurement, in this case the forward outer beam. For clarity only the first six contours of the objective function are plotted here. Every point on the dashed curve is a wind that exactly fits the single observation. The single backscatter observation does not tell us anything



about wind direction since there is a wind solution for every direction, but does strongly indicate a minimum plausible wind speed of  $\approx 10 \text{ m s}^{-1}$ . In other words, the backscatter measurement implies a lower limit of surface roughness. Even if the viewing geometry maximizes the apparent roughness, the wind must be  $\geq 10 \text{ m s}^{-1}$ . On the other hand wind speeds  $> 25 \text{ m s}^{-1}$  are unlikely. The modulation of wind speed with wind direction shown by the dashed curve makes it impossible to deduce an accurate wind speed from the single measurement, but it is this modulation that allows the determination of wind vectors from multiple measurements.

This is seen in Fig. 9.c which shows the result of using both forward and aft outer beam measurements. This scenario is similar to the nominal mode for the 1978 Seasat satellite scatterometer. The dashed curve is as before. Points on the dotted curve exactly fit the aft outer beam observation. Now there are four distinct minima, at the intersections of these two curves, corresponding to four wind ambiguities, plotted here as arrows. In this case, the ambiguities are all perfectly consistent with both measurements. Therefore without additional information, all four are considered to be equally likely. As the wind, viewing geometry, and/or observational errors vary, the two quasi-ellipses may change orientation and aspect ratio leading to zero to four intersections or near intersections, and a corresponding number of wind ambiguities determined.

Finally Fig. 9.d adds the inner beam measurements as well. This is the same situation as in the first panel, but only the first six contours are plotted so that it is possible to see the four curves that give the locus of points that exactly fit each of the four measurements. Wind arrows plotted here are the operational NESDIS NRT retrievals. With the addition of the inner beam measurements, there is less symmetry than in Fig. 9.c, and there are no intersections of all four quasi-ellipses. Also, the minima have become more distinct relative to Fig. 9.c; each minimum is now well separated from the others. In the absence of errors—instrument noise, model function error, etc.—there would be one intersection. In the real data case we must take the minima of the objective function as “best” estimates of the wind. Note that it is now possible to rank the ambiguities by likelihood. The ambiguity with the greatest northward component is most likely. It is this ambiguity, in fact, which is chosen by the ambiguity removal algorithm, and which is consistent with the synoptic situation. This cell is in a broad region of southerly winds and is far to the south of Hurricane Isaac (as seen in Fig. 10).

*b. Swath-dependent characteristics*

The viewing geometry varies across the swath and with the wind direction, resulting in different ambiguity patterns. Some examples are shown in Fig. 10. The upper panel shows a single row of selected wind vectors over the GOES satellite image. For clarity, only wind vectors for even numbered WVCs are plotted. The lower three panels show the objective function at different points across the swath. Cell 38 shows behavior which may be seen close to nadir. In such cases, although 1, 2, 3 or 4 ambiguities may be defined, there is in fact a range of nearly equally likely wind directions and only limited speed information. For cell 38, the wind speed is probably in the range  $3 - 5.5 \text{ m s}^{-1}$  and the wind direction is unlikely to be from the North, but one can say little more. The poor definition of wind direction near nadir is a consequence of having essentially only two azimuth angles. In these cases the quasi-ellipses are well aligned—if they were perfectly aligned, the pattern would reduce to that of a single observation (as in Fig. 9.b). Cell 18 is a good example of the objective function in the “sweet spot” with near-optimal viewing geometry. Four ambiguities are found, and the minima are well-defined. Two minima are dominant and these two are approximately opposed. The direction of the selected ambiguity is easy to verify since the observation is in the environment of Isaac. This is the WVC dissected in Fig. 9. For cell 4, two ambiguities are found and they are approximately opposed. At this point in the far swath, the minima, though clear, are more elongated than in the sweet spot because the diversity of azimuth viewing angles is quite small. This analysis of the QuikSCAT objective function suggests, and comparisons with other data sources show, an increase in the rms speed and directional error near nadir and at the far swath edges.

*c. High and low winds*

Very high and very low winds are also problematic for the scatterometer. The geophysical model function (discussed in Section 2.d) is tuned in part with buoy observations and gridded fields from weather forecast models. Very high winds are underrepresented in these data sets. Consequently, retrieved winds above  $25 \text{ m s}^{-1}$  may be less accurate, and often underestimate the true wind speed (e.g., Hurricane Isaac presented in Section 3).

Low winds have very poor directional skill. Low directional skill is the consequence of a phys-

ical limitation of the instrument’s measurement principle. With no winds, the sea surface is like a smooth reflector, and there is virtually no backscatter. However the scatterometer footprint will usually average over a range of wind speeds (Shankaranarayanan and Donelan 2001). Figure 11 shows the objective function for a very low wind speed case where two of the four  $\sigma^0$  values are negative. Notice that virtually no directional information is present.

Negative  $\sigma^0$  observations are indicative of very light winds. During processing an estimate of the noise is removed from the measurement. Therefore, for low wind speeds, when the true reflected power is very small, the estimated reflected power may be negative (Pierson 1989). The  $\sigma^0$  measurements are stored in  $dB$  and cannot represent negative values. One bit of the  $\sigma^0$  quality flag, denoted  $s$  here, indicates whether the normal (ratio) space  $\sigma^0$  is negative. Thus

$$\sigma^0[\text{ratio}] = (-1)^s 10^{(\sigma^0[dB]/10)}.$$

While negative  $\sigma^0$  are not physically possible, such values are an expected artifact of inverting the model function equation when the signal-to-noise ratio is low. Locations of negative  $\sigma^0$  plotted in red in Fig. 4 (as well as in Fig. 5 and Fig. 6) highlight regions of low wind speed.

#### *d. Rain contamination*

Rainflags have been developed for SeaWinds after the launch of QuikSCAT. Original plans paired SeaWinds with a passive microwave sensor that would have provided a rainflag as was the case with the AMSR on ADEOS-2. Instead for QuikSCAT a variety of alternative rainflags have been proposed, and several of these have been combined into a multi-dimensional histogram (MUDH) rain indicator and rainflag (Huddleston and Stiles 2000). The effect of rain on QuikSCAT wind speed errors varies with the wind magnitude (Weissman et al. 2002). Thus Portabella and Stoffelen (2001) developed a quality control and rain detection procedure for QuikSCAT that applies a wind speed dependent threshold to the normalized QuikSCAT residual. This residual is indicative of the degree of consistency of the observed backscatter and the retrieved wind. Additional rainflags have been developed (e.g. Boukabara et al. 2002) making use of brightness temperature inferred from the SeaWinds noise measurement.

Hoffman et al. (2004) collocated SeaWinds data from QuikSCAT and ADEOS-2 with NCEP Eta analysis winds and with NEXRAD radar estimated rain rates. They found that the rain flag

works well, albeit overly conservatively with too many false alarms. This is especially true when the scatterometer wind speed is high. As the NEXRAD radar estimated rain rate increases, the percent flagged by QuikSCAT increases rapidly. As a result the QuikSCAT rain flags are more accurate for moderate and high rain rates. However the QuikSCAT flags miss many low rain rates observed by NEXRAD radar, and the retrieved wind vectors in these cases are of lower quality.

Figure 12 shows an example of the kind of effect rain can have on QuikSCAT observations. The upper panel shows a highlighted row of selected wind vectors while the lower three panels show objective functions for three WVCs in that row. Cells 41 and 36 are rain free according to the MUDH and NOF rainflags, but cell 40-37 are affected by heavy rain in the front. Notice that the objective function minima in the rain-free cells are very much lower and better defined than in cell 39. Rain has equalized backscatter for cell 39 from all view points and virtually no wind direction signal remains. Also notice rain has nearly doubled the wind speed compared to neighboring rain-free cells.

There is a tendency for wind vectors retrieved in heavy rain to be aligned across the swath (for example in the center of Fig. 5). This occurs because the observed backscatter from the rain is approximately the same for all observing angles (i.e., there is no azimuthal dependence), just the same as when the wind blows across the swath.

## **6. Uses of QuikSCAT data**

QuikSCAT and other scatterometer data have many potential uses. QuikSCAT and other scatterometer data help to detect and precisely locate tropical cyclones (Veldon et al. 2002; Ritchie et al. 2002) and extratropical cyclones. Patterns in scatterometer winds make possible early detection of tropical cyclones and tropical depressions (Katsaros et al. 2001). The method of Sharp et al. (2002) detects tropical cyclones by calculating the vorticity on the SeaWinds WVC grid, and applying a threshold. Zierden et al. (2000) used NSCAT, the precursor to QuikSCAT, to study cyclone surface pressure fields and frontogenesis, and Liu et al. (1997) used NSCAT to monitor the evolution of tropical cyclones. Scatterometer data can be used to specify the radius of gale force winds (Edson and Hawkins 2000), and in addition can depict the two-dimensional patterns of surface wind speed in storms.

QuikSCAT and other scatterometer data are useful for weather analysis and forecasting (Atlas et al. 2001). These data have generally been shown to have a positive impact on Southern Hemisphere extratropics numerical weather prediction (NWP) and a neutral impact on Northern Hemisphere extratropics NWP (e.g., Andrews and Bell 1998), and a positive impact on NWP of tropical cyclones (e.g., Isaksen and Stoffelen 2000; Leidner et al. 2003).

QuikSCAT and other scatterometers also provide fractional coverage of sea ice, monitor large ice bergs in all weather conditions, map different types of ice and snow, and detect the freeze/thaw line in the tundra (Gohin et al. 1998; Ezraty and Cavanie 1999; Remund and Long 1999; Long et al. 2001; Drinkwater et al. 2001).

## 7. Summary

QuikSCAT has provided an extremely accurate and extraordinarily comprehensive view of the surface wind over the global ocean since July 1999 (Chelton et al. 2004). With an 1800 km wide swath QuikSCAT observations cover 90% of the earth every 24 hours. Rms differences between quality controlled research ships and QuikSCAT are roughly speaking  $1 \text{ m s}^{-1}$  in speed and  $15^\circ$  in direction (Bourassa et al. 2003). Scatterometer errors must be smaller than these values since this comparison does not account for collocation errors, differences in scale, or ship observation errors. Although QuikSCAT has exceeded its design lifetime there are no technical reasons that QuikSCAT cannot continue to operate for several additional years.

Optimal use of QuikSCAT winds requires proper quality control based on knowledge of the special characteristics of these data. The two most important quality issues are contamination by rain and ambiguity removal errors. In addition the accuracy of the instrument decreases towards nadir and towards the swath edges. Furthermore wind direction errors are greater for low wind speeds. Validation of the data at high winds is limited. QuikSCAT observations of extreme winds such as in a hurricane are very useful qualitatively but must be treated with caution. In such cases actual numerical values may incorrectly estimate true conditions due to model function errors, instrument limitations, or rain contamination.

The rain flags provided with the data are useful but flag too many high wind speed observations. This is a particularly difficult QC decision since it true both that high winds are often associated

with stormy weather and rain, and that rain contamination can result in higher retrieved scatterometer wind speeds. For heavy rain it is important to note that there is a tendency for retrieved wind vectors to be oriented cross track, because heavy rain and cross track winds result in the same pattern of observed backscatter.

Ambiguity removal errors occur in lines or patches and are often approximate direction reversals. Reported winds may thus have large wind direction errors seemingly corroborated by neighboring WVCs. These errors are a result of the azimuthal response of the scatterometer to the wind roughened ocean and the use of horizontal consistency in the ambiguity removal algorithm. In many situations cloud imagery can be helpful in corroborating rain flags and in detecting ambiguity removal errors.

## **8. Acknowledgments**

The authors thank their colleagues for many helpful discussions. We particularly thank Scott Dunbar (JPL), Julia Figa Saldana (EUMETSAT), and Paul Chang (NOAA/NESDIS). We also thank Rodger Edson (Univ. of Guam/WERI) and Debra K. Smith (RSS) for insight into data quality issues. Mark Cerniglia (AER) provided valuable programming support to create the figures. Data used in the research reported here were provided by the National Environmental Satellite, Data, and Information Service (NESDIS) and the National Centers for Environmental Prediction (NCEP). This research was supported by the NASA Ocean Vector Winds Science Team (OVWST) project.

## A Appendix: Scatterometer objective function

The maximum likelihood estimator maximizes the negative of the objective function depicted in this paper. The objective function is the sum of squared differences between observed and modeled  $\sigma^0$  values, where each squared difference is normalized by its expected variance,  $\varepsilon^2$ . The negative of the objective function, divided by the number of  $\sigma^0$  WVC-composites used, is stored in the NRT data element `max_likelihood_est`. Three coefficients, denoted here as  $\alpha$ ,  $\beta$  and  $\gamma$ , are used to calculate  $\varepsilon^2$ , according to

$$\varepsilon^2 = [\alpha(1 + K_{pm}) - 1](\sigma^0)^2 + \beta\sigma^0 + \gamma.$$

Together the coefficients  $\alpha$ ,  $\beta$  and  $\gamma$  represent the effect of  $K_{pc}$ , the communication noise, and  $K_{pr}$ , the “radar equation” noise due to various geometrical and other instrument uncertainties. Also  $K_{pm}$  accounts for errors in the formulation of the model function. The value of  $\sigma^0$  used here should be the modeled value. That is, during wind inversion, it is the estimate of  $\sigma^0$  based on the current estimate of the wind.

## References

- Andrews, P. L. and R. S. Bell, 1998: Optimizing the United Kingdom Meteorological Office data assimilation for ERS-1 scatterometer winds. *Mon. Wea. Rev.*, **126**, 736–746.
- Atlas, R., S. C. Bloom, R. N. Hoffman, E. Brin, J. Ardizzone, J. Terry, D. Bungato, and J. C. Jusem, 1999: Geophysical validation of NSCAT winds using atmospheric data and analyses. *J. Geophys. Res.*, **104**, 11405–11424.
- , R. N. Hoffman, S. M. Leidner, J. Sienkiewicz, T.-W. Yu, S. C. Bloom, E. Brin, J. Ardizzone, J. Terry, D. Bungato, and J. C. Jusem, 2001: The effects of marine winds from scatterometer data on weather analysis and forecasting. *Bull. Amer. Meteor. Soc.*, **82**, 1965–1990.
- Augenbaum, J. M., R. W. Luczak, and G. Legg, 2004: Seawinds near-real-time scatterometer winds for AWIPS. *20th International Conference on Interactive Information and Processing Systems (IIPS) for Meteorology, Oceanography, and Hydrology*, Seattle, WA, Amer. Meteor. Soc., CD-ROM, 4.10.
- Boukabara, S.-A., R. N. Hoffman, C. Grassotti, and S. M. Leidner, 2002: Physically-based modeling of QSCAT SeaWinds passive microwave measurements for rain detection. *J. Geophys. Res.*, **107**, doi:10.1029/2001JD001243.
- Bourassa, M. A., M. H. Freilich, D. M. Legler, W. T. Liu, and J. J. O’Brien: 1997, Wind observations from new satellite and research vessels agree. *EOS, Trans. Amer. Geophys. Union*, **78**, pp. 597 and 602.
- , D. M. Legler, J. J. O’Brien, and S. R. Smith, 2003: SeaWinds validation with research vessels. *J. Geophys. Res.*, **108**, doi:10.1029/2001JC001028.
- Brown, R. A., 1983: On a satellite scatterometer as an anemometer. *J. Geophys. Res.*, **88**, 1663–1673.
- , 2002: Scaling effects in remote sensing applications and the case of organized large eddies. *The Canadian Journal of Remote Sensing*, **28**, 340–345.



- Chelton, D. B., M. G. Schlax, M. H. Freilich, and R. F. Milliff, 2004: Satellite measurements reveal persistent small-scale features in ocean winds. *Science*, **303**, 978–983.
- Cornillon, P. and K.-A. Park, 2001: Warm core ring velocities inferred from NSCAT. *Geophys. Res. Lett.*, **28**, 575–578.
- Draper, D. W. and D. G. Long, 2002: An assessment of SeaWinds on QuikSCAT wind retrieval. *J. Geophys. Res.*, **107**, doi:10.1029/2002JC001330.
- , and —, 2004: Simultaneous wind and rain retrieval using SeaWinds data. *IEEE Trans. Geosci. Remote Sens.*, **42**, 1411–1423.
- Drinkwater, M. R., D. G. Long, and A. W. Bingham, 2001: Greenland snow accumulation estimates from scatterometer data. *J. Geophys. Res.*, **106**, 33935–33950.
- Edson, R. T. and J. D. Hawkins, 2000: A comparison of scatterometer-derived wind data over tropical cyclones as determined from ERS-2 and QuikSCAT data. *24th Conference on Hurricanes and Tropical Meteorology*, Fort Lauderdale, FL, Amer. Meteor. Soc., 195–196.
- Ezraty, R. and A. Cavanie, 1999: Intercomparison of backscatter maps over Arctic sea ice from NSCAT and the ERS scatterometer. *J. Geophys. Res.*, **104**, 11471–11483.
- Freilich, M. H., 2000: Seawinds: Algorithm theoretical basis document. Technical report, Oregon State University, Corvallis, 56 pp.
- , and R. S. Dunbar, 1993: Derivation of satellite wind model functions using operational surface wind analyses: An altimeter example. *J. Geophys. Res.*, **98**, 14633–14649.
- , and —, 1999: The accuracy of the NSCAT 1 vector winds: Comparisons with National Data Buoy Center buoys. *J. Geophys. Res.*, **104**, 11231–11246.
- Gohin, F., A. Cavanie, and R. Ezraty, 1998: Evolution of the passive and active microwave signatures of a large sea ice feature during its  $2\frac{1}{2}$ -year drift through the Arctic Ocean. *J. Geophys. Res.*, **103**, 8177–8189.

- Heirtzler, J. R., 2002: The future of the South Atlantic anomaly and implications for radiation damage in space. *Journal of Atmospheric and Terrestrial Physics*, **64**, 1701–1708.
- Henderson, J. M., R. N. Hoffman, S. M. Leidner, J. V. Ardizzone, R. Atlas, and E. Brin, 2003: A comparison of a two-dimensional variational analysis method and a median filter for NSCAT ambiguity removal. *J. Geophys. Res.*, **108**, 3176, doi:10.1029/2002JC001307.
- Hoffman, R. N., and J.-F. Louis, 1990: The influence of atmospheric stratification on scatterometer winds. *J. Geophys. Res.*, **95**, 9723–9730.
- , C. Grassotti, and S. M. Leidner, 2004: Seawinds validation: Effect of rain as observed by East Coast radars. *J. Atmos. Oceanic Technol.*, **21**, 1364–1377.
- , S. M. Leidner, J. M. Henderson, R. Atlas, J. V. Ardizzone, and S. C. Bloom, 2003: A two-dimensional variational analysis method for NSCAT ambiguity removal: Methodology, sensitivity, and tuning. *J. Atmos. Oceanic Technol.*, **20**, 585–605.
- Huddleston, J. N. and B. W. Stiles, 2000: A multidimensional histogram rain-flagging technique for SeaWinds on QuikSCAT. *Proc. Int. Geoscience and Remote Sensing Symp. (IGARSS)*, Honolulu, HI, Institute of Electrical and Electronics Engineers, 1232–1234.
- Isaksen, L. and A. Stoffelen, 2000: ERS scatterometer wind data impact on ECMWF’s tropical cyclone forecasts. *IEEE Trans. Geosci. Remote Sens.*, **38**, 1885–1892.
- Jones, W. L., V. J. Cardone, W. J. Pierson, J. Zec, L. P. Rice, A. Cox, and W. B. Sylvester, 1999: NSCAT high-resolution surface wind measurements in Typhoon Violet. *J. Geophys. Res.*, **104**, 11247–11259, correction in number C8, page 18,469.
- Katsaros, K. B., E. B. Forde, P. Chang, and W. T. Liu, 2001: QuikSCAT’s SeaWinds facilitates early identification of tropical depressions in 1999 hurricane season. *Geophys. Res. Lett.*, **28**, 1043–1046.
- Leidner, S., M. Cerniglia, and R. N. Hoffman, 2001: Comparison of ambiguity removal for science and near-real time SeaWinds data. *EOS, Trans. Amer. Geophys. Union*, **82**, Fall Meet. Suppl., Abstract OS31A-0381.

- , R. N. Hoffman, and J. Augenbaum, 2000: *SeaWinds Scatterometer Real-Time BUFR Geophysical Data Product*. Atmospheric and Environmental Research, Inc., Cambridge, MA, version 2.3.0, 45 pp.
- , L. Isaksen, and R. N. Hoffman, 2003: Impact of NSCAT winds on tropical cyclones in the ECMWF 4D-Var assimilation system. *Mon. Wea. Rev.*, **131**, 3–26.
- Liu, W. T., W. Tang, and R. S. Dunbar, 1997: Scatterometer observes extratropical transition of Pacific typhoons. *EOS, Trans. Amer. Geophys. Union*, **78**, pp. 237 and 240.
- Long, D. G., M. R. Drinkwater, B. Holt, S. Saatchi, and C. Bertoia, 2001: Global ice and land climate studies using scatterometer image data. *EOS, Trans. Amer. Geophys. Union*, **82**, 503.
- Lungu, T., Ed., 2001: QuikSCAT science data product user's manual, overview and geophysical data products. Version 2.2, Jet Propulsion Laboratory, Pasadena, CA, 95 pp. [JPL D-18053.]
- Mears, C. A., D. K. Smith, and F. J. Wentz, 2001: Comparison of Special Sensor Microwave Imager and buoy-measured wind speeds from 1987 to 1997. *J. Geophys. Res.*, **106**, 11719–11729.
- Peteherych, S., P. M. Woiceshyn, W. Appleby, L. Chu, J. Spagnol, and J. E. Overland, 1981: High resolution marine meteorological analysis utilizing Seasat data. *Oceanography from Space*, J. F. R. Gower, Ed., Plenum, 581–586.
- Pierson, W. J., Jr., 1989: Probabilities and statistics for backscatter estimates obtained by a scatterometer. *J. Geophys. Res.*, **94**, 9743–9759.
- Portabella, M. and A. Stoffelen, 2001: On quality control and rain detection of SeaWinds. *J. Atmos. Oceanic Technol.*, **18**, 1171–1183.
- , and —, 2004: A probabilistic approach for SeaWinds data assimilation. *Quart. J. Roy. Meteor. Soc.*, **130**, 127–152.
- Quilfen, Y., B. Chapron, and D. Vandemark, 2001: The ERS scatterometer wind measurement accuracy: Evidence of seasonal and regional biases. *J. Atmos. Oceanic Technol.*, **18**, 1684–1697.

- Remund, Q. P. and D. G. Long, 1999: Sea ice extent mapping using Ku band scatterometer data. *J. Geophys. Res.*, **104**, 11515–11527.
- Ritchie, E., J. Simpson, W. T. Liu, C. Veldon, K. Brueske, and J. Halvorsen, 2002: A closer look at hurricane formation and intensification using new technology. *Coping with Hurricanes*, R. Simpson, M. Garstang, and R. Anthes, Eds., American Geophysical Society, Washington, DC, pp. 249–290.
- Shaffer, S. J., R. S. Dunbar, S. V. Hsiao, and D. G. Long, 1991: A median-filter-based ambiguity removal algorithm for NSCAT. *IEEE Trans. Geosci. Remote Sens.*, **29**, 167–174.
- Shankaranarayanan, K. and M. A. Donelan, 2001: A probabilistic approach to scatterometer model function verification. *J. Geophys. Res.*, **106**, 19969–19990.
- Sharp, R. J., M. A. Bourassa, and J. J. O'Brien, 2002: Early detection of tropical cyclones using SeaWinds-derived vorticity. *Bull. Amer. Meteor. Soc.*, **83**, 879–889.
- Sobieski, P. W., C. Craeye, and L. F. Bliven, 1999: Scatterometric signatures of multivariate drop impacts on fresh and salt water surfaces. *Int. J. Remote Sens.*, **20**, 2149–2166.
- Spencer, M. W., C. Wu, and D. G. Long, 2000: Improved resolution backscatter measurements with the SeaWinds pencil-beam scatterometer. *IEEE Trans. Geosci. Remote Sens.*, **38**, 89–104.
- Stiles, B. W., B. D. Pollard, and R. S. Dunbar, 2002: Direction interval retrieval with thresholded nudging: A method for improving the accuracy of QuickSCAT winds. *IEEE Trans. Geosci. Remote Sens.*, **40**, 79–89.
- Stoffelen, A., 1998: Toward the true near-surface wind speed: Error modeling and calibration using triple collocation. *J. Geophys. Res.*, **103**, 7755–7766.
- Thorpe, W., 1995: A guide to the WMO code form FM 94 BUFR. Technical Report FM-I6-1995, Office of the Federal Coordinator for Meteorological Services and Supporting Research, NOAA, Silver Springs, Maryland, 122 pp.

- Uhlhorn, E. W. and P. G. Black, 2003: Verification of remotely sensed sea surface winds in hurricanes. *J. Atmos. Oceanic Technol.*, **20**, 99–116.
- Veldon, C., K. Bruske, C. Kummerow, W. T. Liu, J. Simpson, S. Braun, and R. Anthes, 2002: The burgeoning role of weather satellites. *Coping with Hurricanes*, R. Simpson, M. Garstang, and R. Anthes, eds., American Geophysical Society, Washington, DC, pp. 217–218.
- Weissman, D. E., M. A. Bourassa, and J. Tongue, 2002: Effects of rain rate and wind magnitude on SeaWinds scatterometer wind speed errors. *J. Atmos. Oceanic Technol.*, **19**, 738–746.
- Wentz, F. J. and D. K. Smith, 1999: A model function for the ocean-normalized radar cross section at 14 GHz derived from NSCAT observations. *J. Geophys. Res.*, **104**, 11499–11514.
- Yu, T.-W. and V. M. Gerald, 2004: Evaluation of NCEP operational model forecasts of surface wind and pressure fields over the oceans. *20th Conference on Weather Analysis and Forecasting/16th Conference on Numerical Weather Prediction*, Seattle, WA, Amer. Meteor. Soc., Boston, MA, CD-ROM, P4.18.
- Yueh, S. H., B. W. Stiles, W.-Y. Tsai, H. Hu, and W. T. Liu, 2001: QuikSCAT geophysical model function for tropical cyclones and application to Hurricane Floyd. *IEEE Trans. Geosci. Remote Sens.*, **39**, 2601–2612.
- Zierden, D. F., M. A. Bourassa, and J. J. O'Brien, 2000: Cyclone surface pressure fields and frontogenesis from NASA Scatterometer (NSCAT). *J. Geophys. Res.*, **105**, 23967–23981.

## TABLE LEGENDS

**Table 1:** Mean and standard deviation of differences between the selected scatterometer wind observations and the background ( $O - B$ ) and between the selected scatterometer wind observations and the analysis ( $O - A$ ) for the ALLOBS and NORAIN analyses in the North Atlantic valid 2100 UTC 28 Sep 2000.

## FIGURE LEGENDS

**Fig. 1:** Global QuikSCAT wind data coverage for 1 November 2000. WVCs that contain retrieved winds from 0104 UTC 1 November until 0041 UTC 2 November are first plotted in dark blue for descending parts of orbits, then light blue for ascending parts of orbits, and finally green for a single data segment. The green highlighted segment covers the period 0145 to 0300 UTC. For this segment the WVC rows near the midpoint of the data overlap region are colored black. (The midpoint in the Persian Gulf is mostly obscured by land.) White areas indicates no QuikSCAT wind data because of no data coverage, insufficient  $\sigma^0$  diversity, or the presence of ice.

**Fig. 2:** The SeaWinds instrument on QuikSCAT. The rotating disk antenna is 1 m in diameter (courtesy NASA/JPL).

**Fig. 3:** A schematic of the measurement geometry of the SeaWinds instrument on QuikSCAT (from Freilich 2000). As indicated on the figure the far swath extends from 700 to 900 km on either side. The nadir swath is 400 km wide, centered on nadir.

**Fig. 4:** QuikSCAT winds, NCEP GFS sea-level pressure analysis, and GOES satellite infrared image over the western North Atlantic close to 2200 UTC 28 September 2000. The QuikSCAT data swath represents about 12 minutes of data collected during rev 6659 centered at 2207 UTC. Winds are plotted using standard wind barb notation with short, long, and filled triangle flags indicating 5, 10, and 50 kt (2.57, 5.14, and 25.72 m s<sup>-1</sup>). Rain-flagged winds are green. Red dots indicate the locations of negative  $\sigma^0$  observations. For clarity the QuikSCAT winds have been thinned to every fourth WVC along- and across-track. The NCEP GFS mean sea-level pressure analysis valid 0000 UTC 29 September is contoured every 2 hPa. The GOES image valid 2215 UTC is shaded according to the gray scale on the right.

**Fig. 5:** Same as Fig. 4 but for winds around Hurricane Isaac at full resolution. The red square indicates the best track position at the time of the GOES image.

**Fig. 6:** Same as Fig. 4 but for winds around a front in the northwestern North Atlantic at full resolution.

**Fig. 7:** Histograms of differences of QuikSCAT selected winds from the background (left) and the NORAIN 2d-VAR analysis (right).

**Fig. 8:** An example of the impact of QuikSCAT data on a variational analysis. Upper left panel shows a portion of the background wind field used in 2d-VAR in the vicinity of a synoptic front. The background field is a 3-hour NCEP GFS forecast, valid at 2100 UTC 28 September 2000. Streamlines are plotted to highlight instantaneous features in the flow. The middle and lower left panels show 2d-VAR ALLOBS and NORAIN analyses, respectively. The right panels correspond to the area of the orange dashed boxes drawn in the left panels and show QuikSCAT ambiguities over the GOES image and the sea-level pressure analysis of Fig. 4 except that the contour interval is 0.5 hPa. The top left panel shows directions, but not speeds, for all ambiguities. The middle and lower left panels show the ambiguities closest to the ALLOBS and NORAIN analyses, respectively. Rain-flagged winds are green.

**Fig. 9:** The QuikSCAT objective function (dimensionless) plotted as a function of  $u$  and  $v$  wind components (in  $\text{m s}^{-1}$  on the abscissa and ordinate, respectively). The wind solutions are plotted as arrows, and the selected ambiguity is plotted with a thick line. The data used are from the NRT product for rev 6659, row 1100, cell 18, observed 2207 UTC 28 September 2000. Panel a considers all four backscatter observations, and is plotted using the conventions of all similar figures that follow. Contours with values 1, 2, 3, 5, 7 are blue, 10, 20, 30, 50, 70 are green, and 100, 200, 300, 500 are orange. Values 700 and higher are filled in with red. Panels b–d show the QuikSCAT objective function for a single backscatter observation, two, and then all four, respectively. Only the lowest six contours are plotted in these panels. The locus of  $(u, v)$  which exactly fit each backscatter observation is plotted as a dotted or dashed curve in panels b–d. Dashed (dotted) curves correspond to forward-looking (aft-looking) observations. Black loci curves denote observations made by the



outer beam, while red loci curves denote observations made by the inner beam. For reference, in panel a, the global minimum of the objective function is  $8.7 \times 10^{-6}$ . It attains a value of  $2.6 \times 10^5$  at the origin in  $(u, v)$  space.

**Fig. 10:** The QuikSCAT objective function showing different ambiguity patterns. These data are for rev 6659, row 1100, and cells 38, 18, and 4. For reference the selected wind vectors for the even-numbered WVCs in row 1100 are plotted over the GOES image. Objective function plots as in Fig. 9.a.

**Fig. 11:** The QuikSCAT objective function for a very low winds case. The example is cell 48 from the wind vector cell row presented in the previous figure (Fig. 10, upper panel). The four observed  $\sigma^0$  values multiplied by  $10^6$  and ordered as they were measured by QuikSCAT are: outer-fore 56, inner-fore: -40, inner-aft: 42 and outer-aft: -15.

**Fig. 12:** An example of rain-contaminated winds from QuikSCAT. The upper panel shows the wind vector cell row of interest in bold wind barbs. Rain-flagged winds are green. The panels below show the QuikSCAT objective function for cells 41, 39 and 36.

## TABLES

**Table 1:** Mean and standard deviation of differences between the selected scatterometer wind observations and the background ( $O - B$ ) and between the selected scatterometer wind observations and the analysis ( $O - A$ ) for the ALLOBS and NORAIN analyses in the North Atlantic valid 2100 UTC 28 Sep 2000.

Case	$N$	Difference	Mean	std dev
ALLOBS	12004	$O - B$	0.846	2.571
		$O - A$	0.288	2.037
NORAIN	10754	$O - B$	0.412	1.833
		$O - A$	0.179	1.279

## FIGURES

**Fig. 1:** Global QuikSCAT wind data coverage for 1 November 2000. WVCs that contain retrieved winds from 0104 UTC 1 November until 0041 UTC 2 November are first plotted in dark blue for descending parts of orbits, then light blue for ascending parts of orbits, and finally green for a single data segment. The green highlighted segment covers the period 0145 to 0300 UTC. For this segment the WVC rows near the midpoint of the data overlap region are colored black. (The midpoint in the Persian Gulf is mostly obscured by land.) White areas indicates no QuikSCAT wind data because of no data coverage, insufficient  $\sigma^0$  diversity, or the presence of ice.

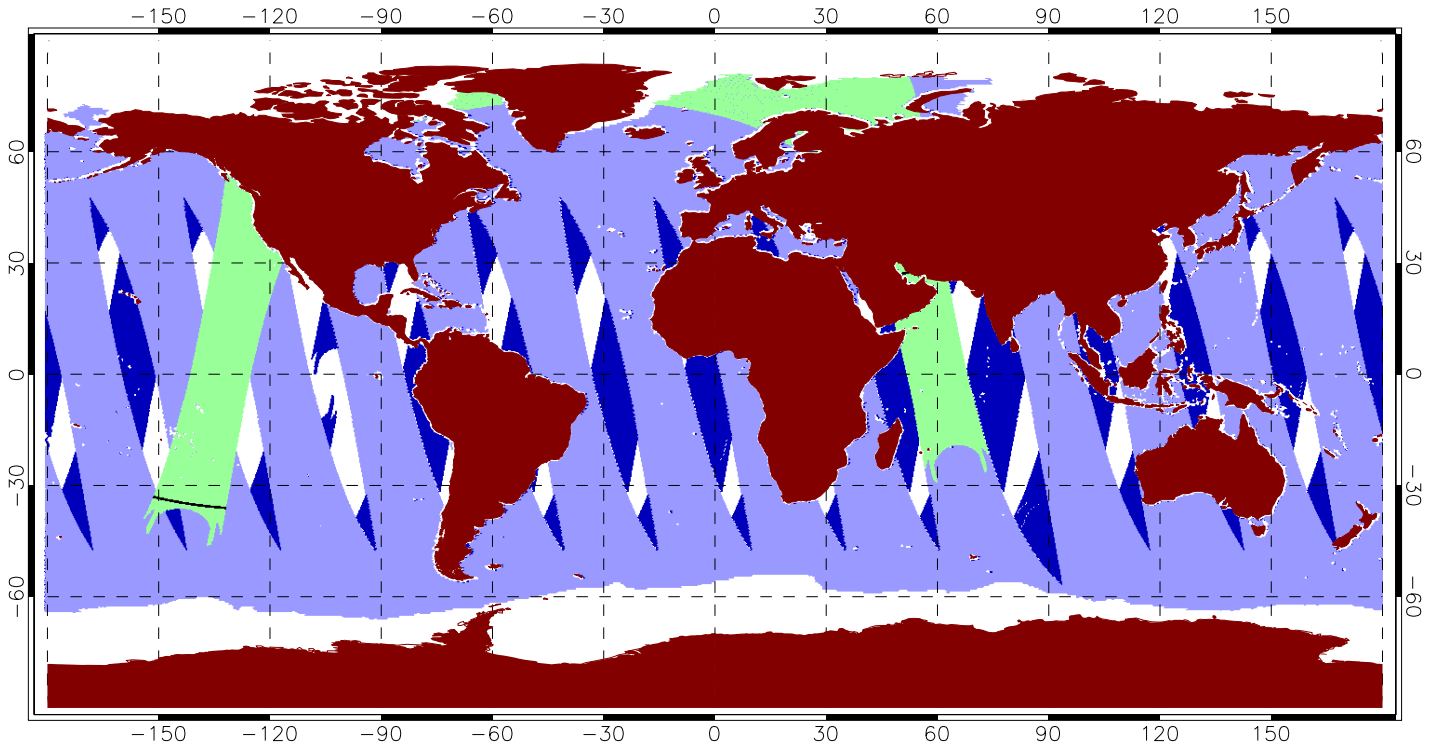


**Fig. 2:** The SeaWinds instrument on QuikSCAT. The rotating disk antenna is 1 m in diameter (courtesy NASA/JPL).



**Fig. 3:** A schematic of the measurement geometry of the SeaWinds instrument on QuikSCAT (from Freilich 2000). As indicated on the figure the far swath extends from 700 to 900 km on either side. The nadir swath is 400 km wide, centered on nadir.

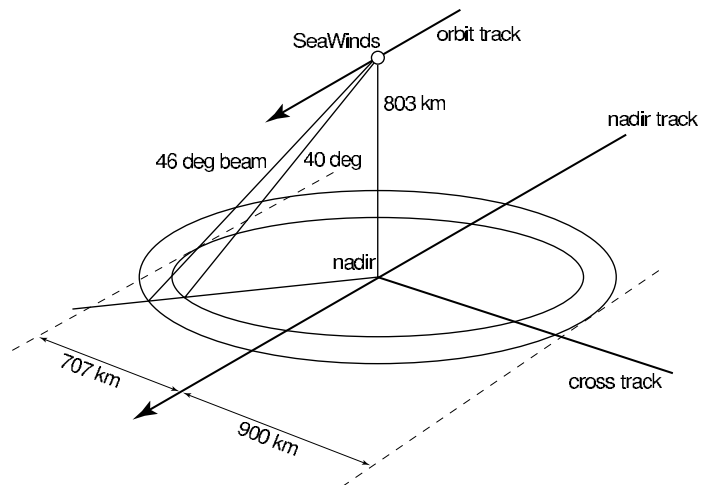


**Fig. 4:** QuikSCAT winds, NCEP GFS sea-level pressure analysis, and GOES satellite infrared image over the western North Atlantic close to 2200 UTC 28 September 2000. The QuikSCAT data swath represents about 12 minutes of data collected during rev 6659 centered at 2207 UTC. Winds are plotted using standard wind barb notation with short, long, and filled triangle flags indicating 5, 10, and 50 kt ( $2.57$ ,  $5.14$ , and  $25.72$   $\text{m s}^{-1}$ ). Rain-flagged winds are green. Red dots indicate the locations of negative  $\sigma^0$  observations. For clarity the QuikSCAT winds have been thinned to every fourth WVC along- and across-track. The NCEP GFS mean sea-level pressure analysis valid 0000 UTC 29 September is contoured every 2 hPa. The GOES image valid 2215 UTC is shaded according to the gray scale on the right.

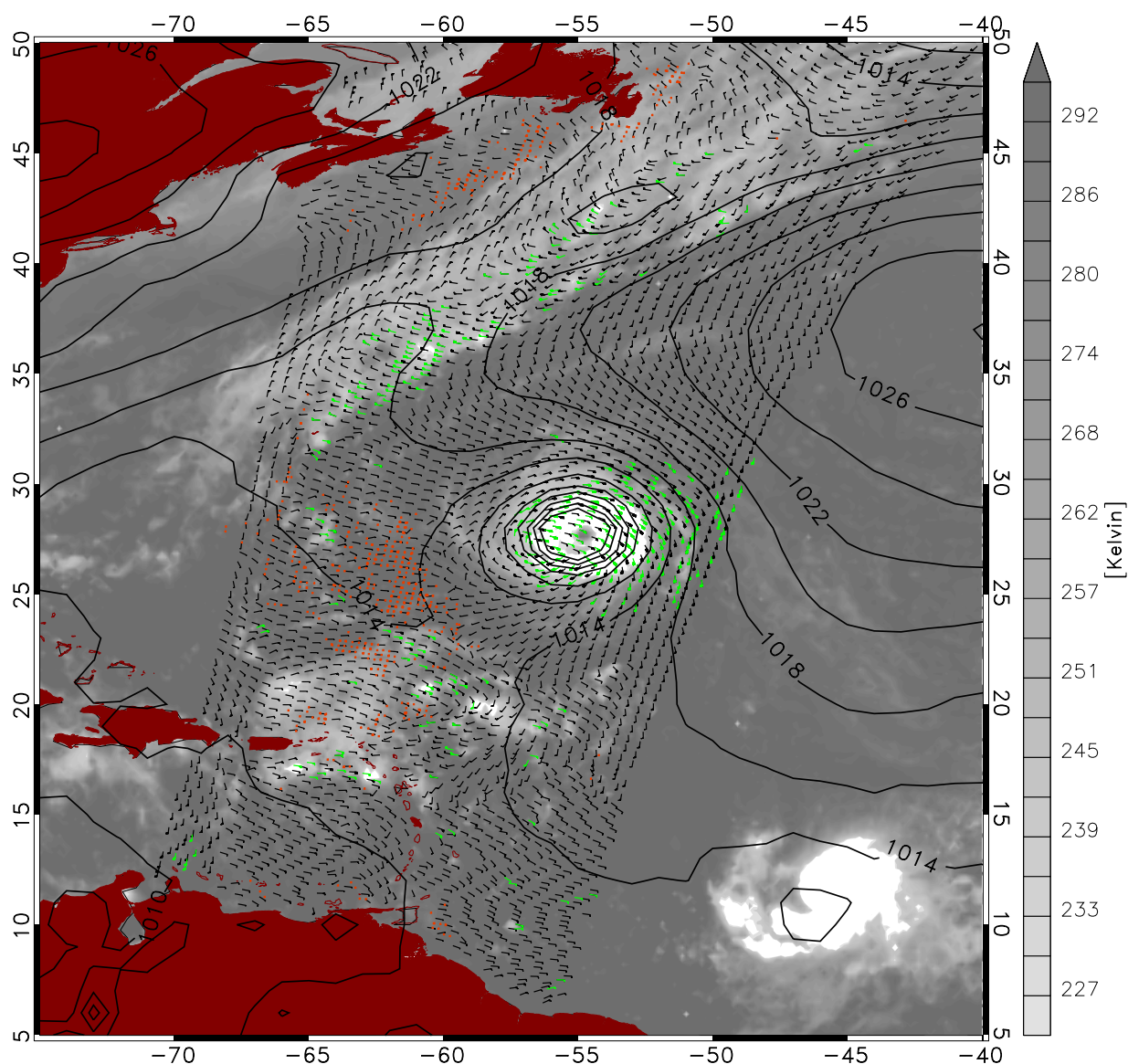


**Fig. 5:** Same as Fig. 4 but for winds around Hurricane Isaac at full resolution. The red square indicates the best track position at the time of the GOES image.

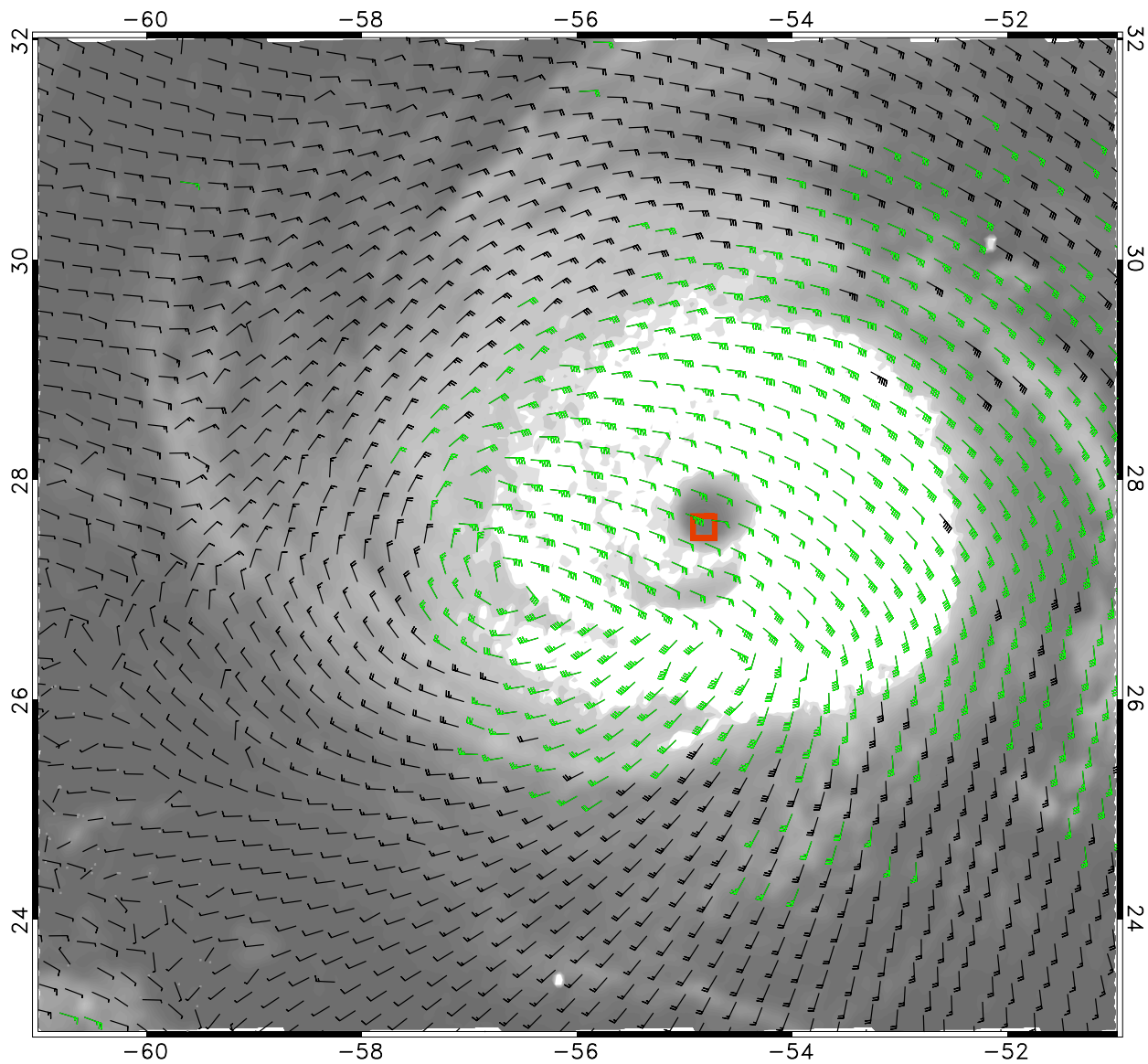




**Fig. 6:** Same as Fig. 4 but for winds around a front in the northwestern North Atlantic at full resolution.

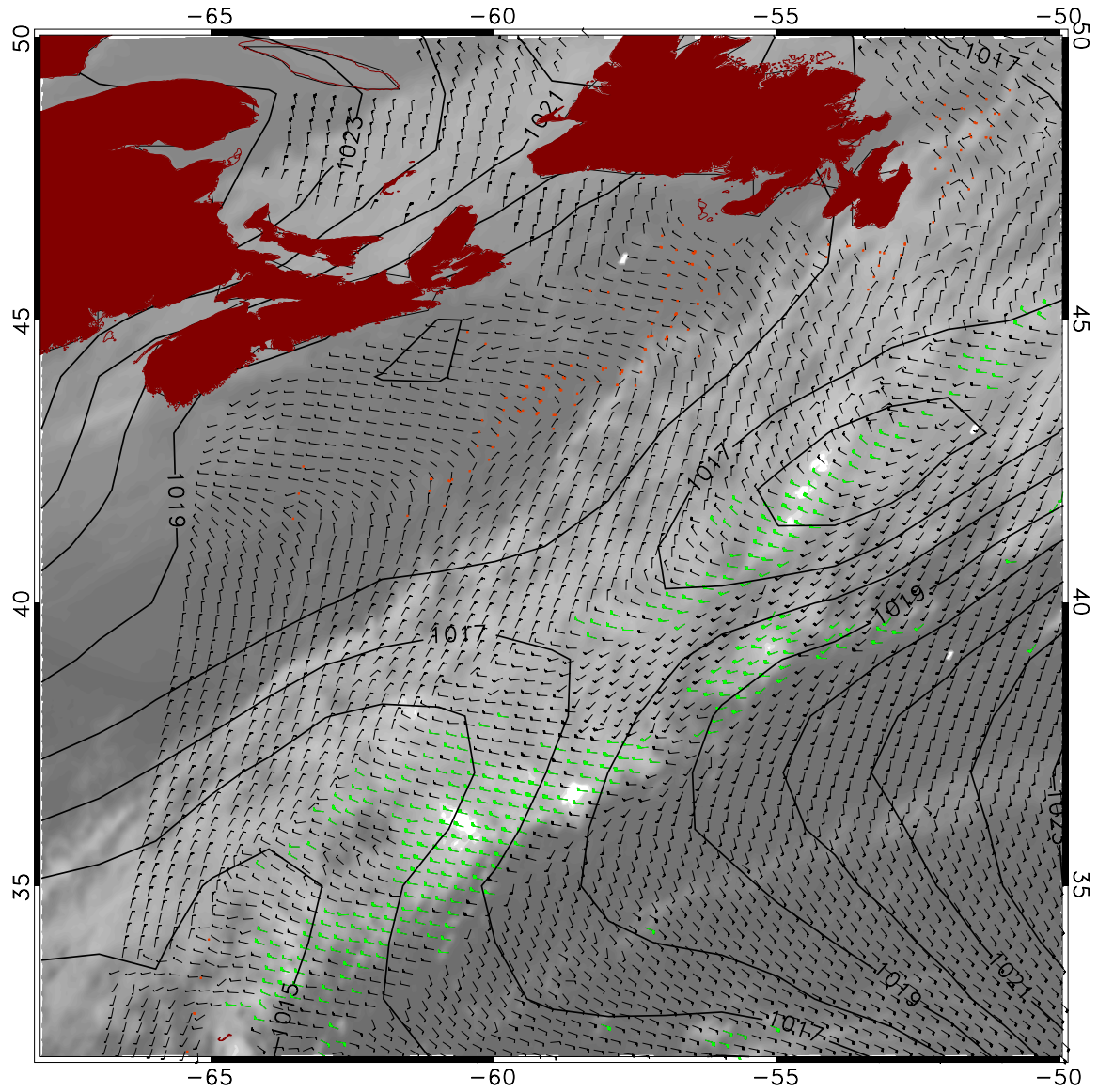


**Fig. 7:** Histograms of differences of QuikSCAT selected winds from the background (left) and the NORAIN 2d-VAR analysis (right).

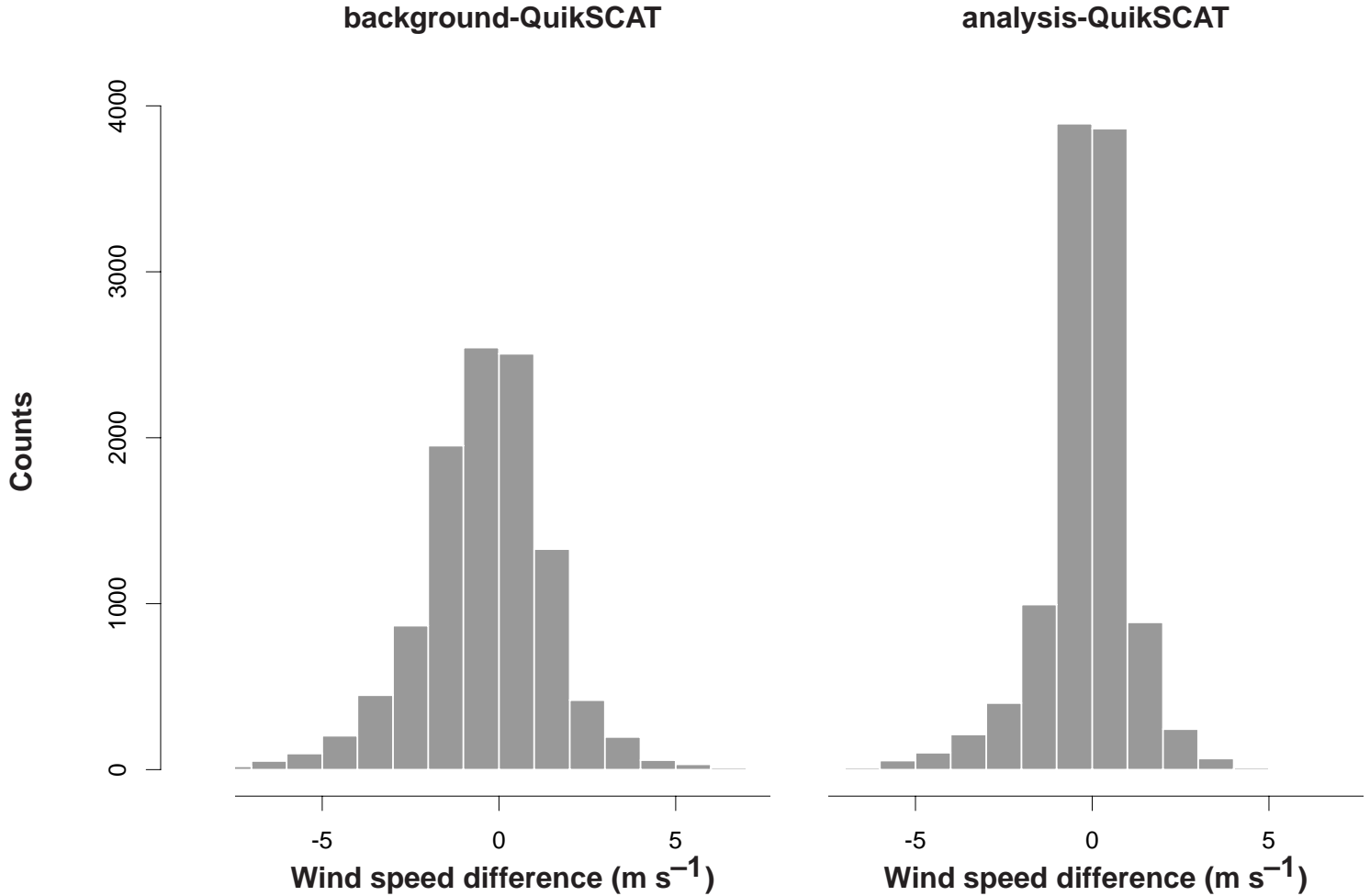
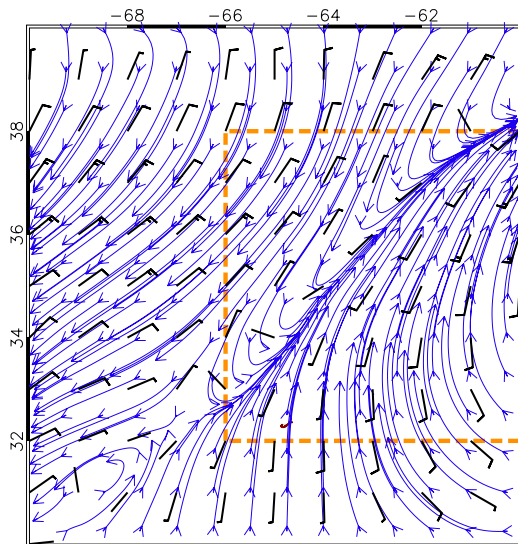


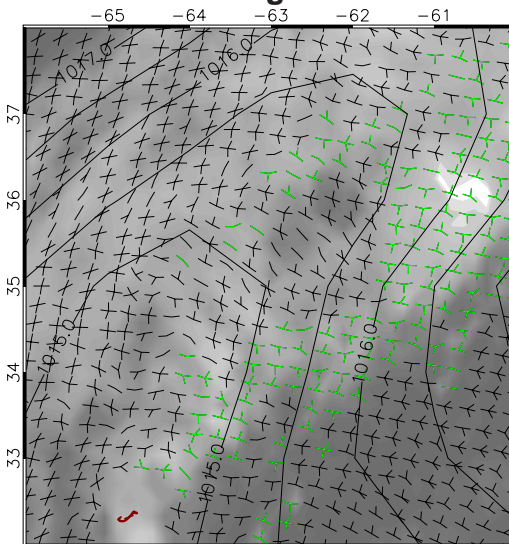
**Fig. 8:** An example of the impact of QuikSCAT data on a variational analysis. Upper left panel shows a portion of the background wind field used in 2d-VAR in the vicinity of a synoptic front. The background field is a 3-hour NCEP GFS forecast, valid at 2100 UTC 28 September 2000. Streamlines are plotted to highlight instantaneous features in the flow. The middle and lower left panels show 2d-VAR ALLOBS and NORAIN analyses, respectively. The right panels correspond to the area of the orange dashed boxes drawn in the left panels and show QuikSCAT ambiguities over the GOES image and the sea-level pressure analysis of Fig. 4 except that the contour interval is 0.5 hPa. The top left panel shows directions, but not speeds, for all ambiguities. The middle and lower left panels show the ambiguities closest to the ALLOBS and NORAIN analyses, respectively. Rain-flagged winds are green.



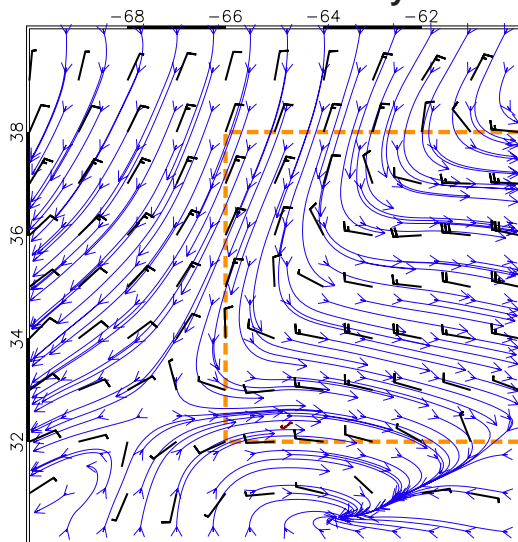
**First Guess**



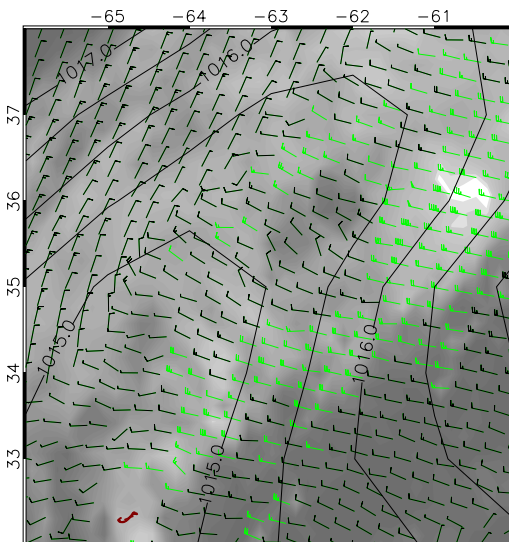
**All ambiguities**



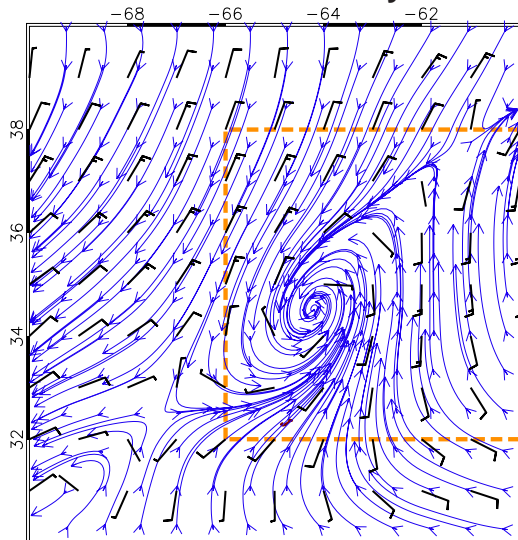
**2d-VAR ALLOBS Analysis**



**Closest to ALLOBS**



**2d-VAR NORAIN Analysis**



**Closest to NORAIN**

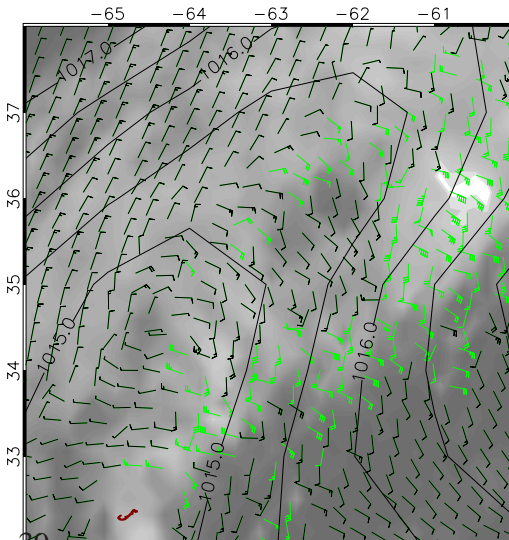


**Fig. 9:** The QuikSCAT objective function (dimensionless) plotted as a function of  $u$  and  $v$  wind components (in  $\text{m s}^{-1}$  on the abscissa and ordinate, respectively). The wind solutions are plotted as arrows, and the selected ambiguity is plotted with a thick line. The data used are from the NRT product for rev 6659, row 1100, cell 18, observed 2207 UTC 28 September 2000. Panel a considers all four backscatter observations, and is plotted using the conventions of all similar figures that follow. Contours with values 1, 2, 3, 5, 7 are blue, 10, 20, 30, 50, 70 are green, and 100, 200, 300, 500 are orange. Values 700 and higher are filled in with red. Panels b–d show the QuikSCAT objective function for a single backscatter observation, two, and then all four, respectively. Only the lowest six contours are plotted in these panels. The locus of  $(u, v)$  which exactly fit each backscatter observation is plotted as a dotted or dashed curve in panels b – d. Dashed (dotted) curves correspond to forward-looking (aft-looking) observations. Black loci curves denote observations made by the outer beam, while red loci curves denote observations made by the inner beam. For reference, in panel a, the global minimum of the objective function is  $8.7 \times 10^{-6}$ . It attains a value of  $2.6 \times 10^5$  at the origin in  $(u, v)$  space.

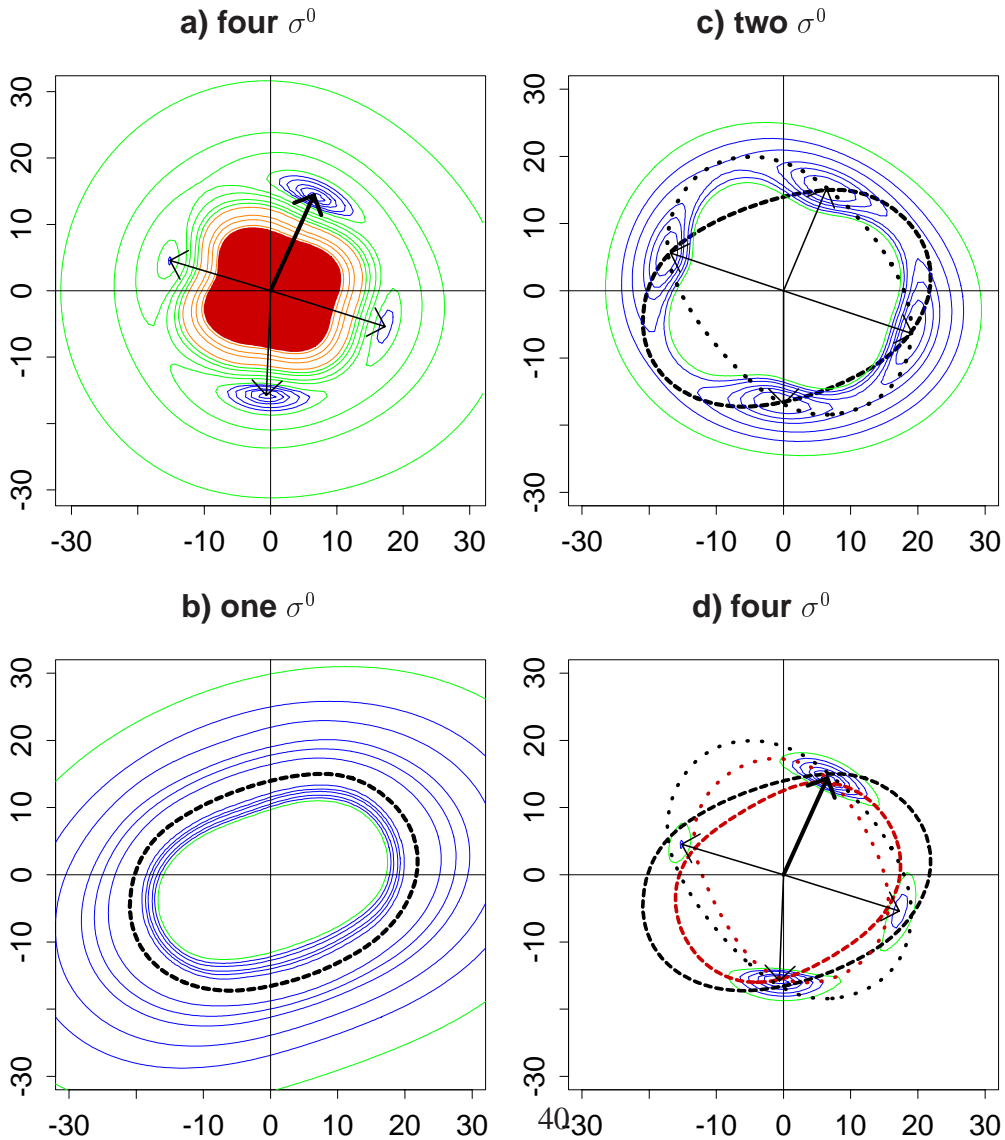


**Fig. 10:** The QuikSCAT objective function showing different ambiguity patterns. These data are for rev 6659, row 1100, and cells 38, 18, and 4. For reference the selected wind vectors for the even-numbered WVCs in row 1100 are plotted over the GOES image. Objective function plots as in Fig. 9.a.

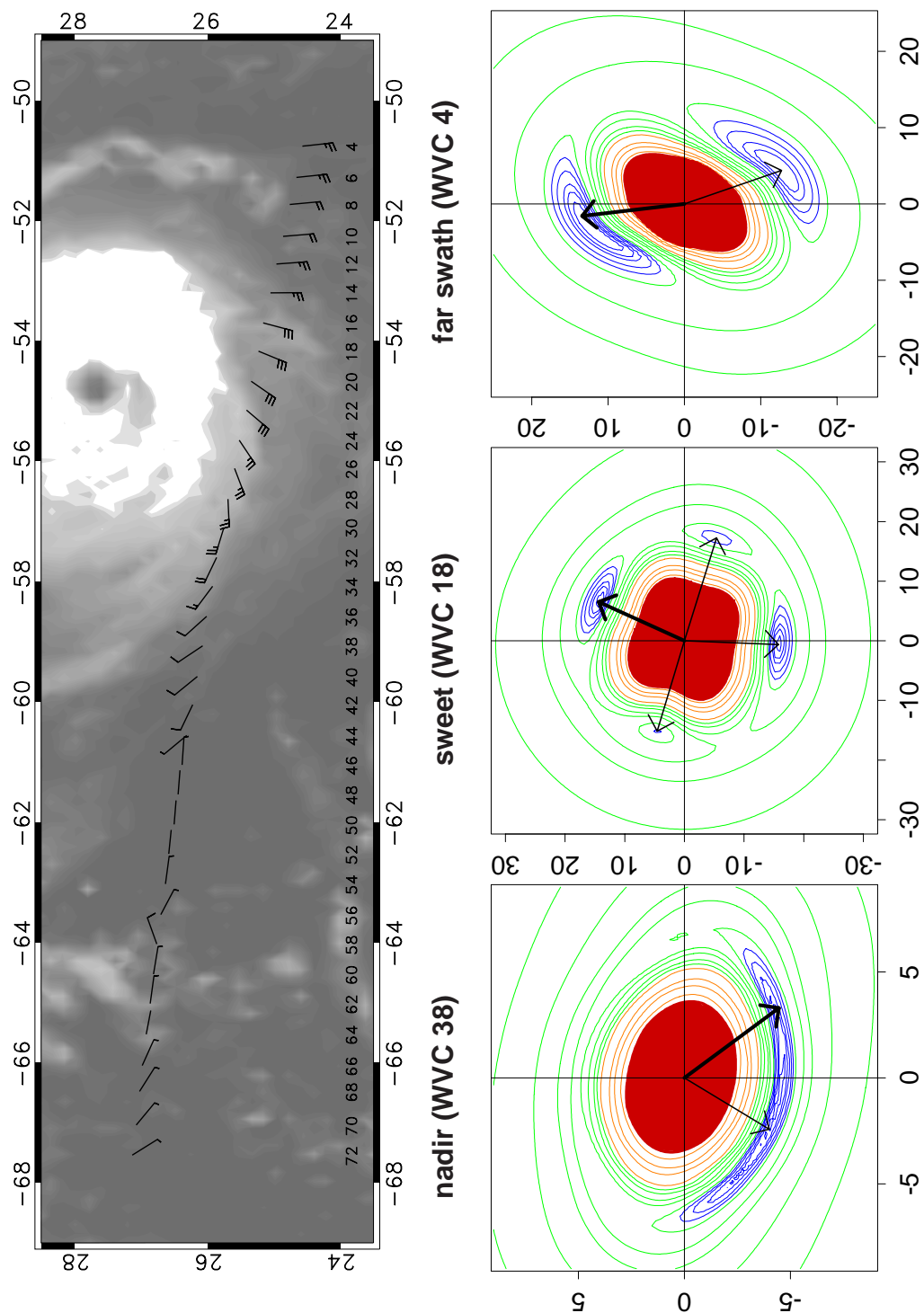


**Fig. 11:** The QuikSCAT objective function for a very low winds case. The example is cell 48 from the wind vector cell row presented in the previous figure (Fig. 10, upper panel). The four observed  $\sigma^0$  values multiplied by  $10^6$  and ordered as they were measured by QuikSCAT are: outer-fore 56, inner-fore: -40, inner-aft: 42 and outer-aft: -15.

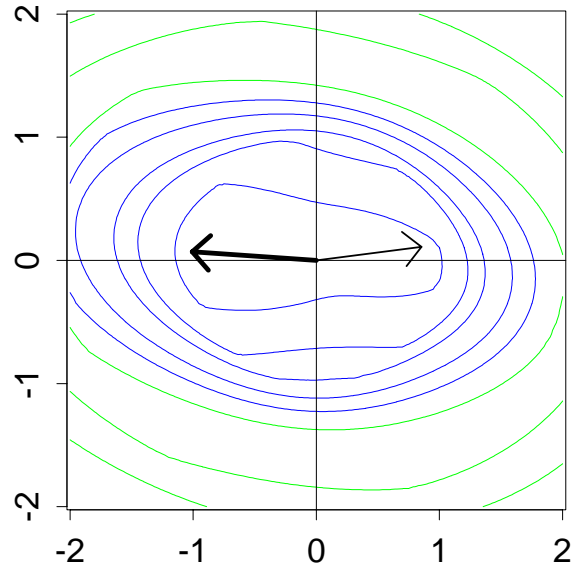


**Fig. 12:** An example of rain-contaminated winds from QuikSCAT. The upper panel shows the wind vector cell row of interest in bold wind barbs. Rain-flagged winds are green. The panels below show the QuikSCAT objective function for cells 41, 39 and 36.

